Thermal Imaging Analysis of Rockfalls Leading to Slope Failures at an Open-Pit Mine

K.W. Schafer University of Arizona, Tucson, Arizona

E.C Wellman, G.E. Noonan & B.J. Ross University of Arizona, Tucson, Arizona

C.P. Williams, K. Bakken, G. Abrahams, & D. Hicks, Rio Tinto Kennecott Copper, Salt Lake City Utah

Abstract

Rockfalls are both abrupt and potentially hazardous events at open-pit mines. The Geotechnical Center of Excellence (GCE) within the Lowell Institute for Mineral Resources at the University of Arizona has evaluated the use of thermal cameras to detect and record rockfalls prior a large slope failure and an additional, secondary failure of the same slope. The timing of both the initial and secondary failures were well-predicted by the mine operator's integrated monitoring system that includes state-of-the-art radar systems. Continuous thermal videos are available before, during, and after both slope failures.

Video recording of the deforming slope began on May 27, 2021, approximately 4 days before the initial, Leo Failure. From May 29, monitoring of the thermal camera data indicated that rockfalls increased in frequency from approximately 5 to 20 per day. Many rockfalls were spatially coincident with the outline of the ultimate failure scarp. Post-failure, video-review and interpretations indicate an exponential increase in cumulative rockfalls leading to slope failure, with approximately 45% of the total interpreted rockfalls (158) occurring within 6 hours of the primary failure. A post-failure video-review of the 3-4 days leading up to the secondary failure indicates a similar cumulative rockfall behavior with approximately 40% of the total interpreted rockfalls (262) occurring over the 6 hours leading to the secondary failure.

The cumulative rockfall curves for the failures exhibit behavior similar to time-dependent, displacement curves (sensu Broadbent & Zavodni, 1982) where increases or decreases in rockfall frequency, may be considered a proxy for progressive or regressive stage developments, respectively.

This paper will discuss how rockfall data from the thermal video can potentially be used alongside other slope monitoring data (e.g., radar) to predict the timing of slope failures.

1 Introduction

A 'rockfall' generally refers to downslope rolling, tumbling, and translating of inch to ft-scale (cm to m-scale) rocks. Rockfalls are a ubiquitous safety concern at active mine slopes where the presence of both personnel and equipment are at risk. Rockfalls are transient phenomena that can result from a wide range of conditions present in surface mining; e.g., poor blasting and scaling; degradation associated with surface weathering phenomena such as surface water runoff or freeze-thaw spalling (Read & Stacey, 2009). More importantly, rockfalls can be precursory events to larger-scale failures (Rosser et al., 2007; Kromer et al., 2015) that could pose a significant risk to both personnel and equipment; and potentially diminish the economic value of a mining operation.

The collapse/failure of an open-pit slope generally adheres to a three-phase cyclicity of time-dependent displacement (Broadbent & Zavodoni, 1983; Zavodoni, 2001). This cycle is remarkably similar to time-dependent strain measured in laboratory, rock-deformation creep experiments (e.g., Hobbs et al., 1976; Byerlee, 1978): An initial, transient acceleration of strain-rate (primary creep); followed by a regression (de-acceleration) in strain-rate leading to steady-state (secondary creep); followed, in-turn, by a final progressive strain acceleration ultimately leading to slope collapse (tertiary creep). Most case-studies of slope-collapse use a measure of slope movement, such as displacement, to describe either a power or exponential trend to the progressive (tertiary creep) final phase of damage accumulation leading to megascopic brittle failure. A common practice is to invert the final, progressive-stage velocities and fit a straight line in velocity^{-1} (1/velocity) vs time-space where the horizontal axis (time) intercept is the time at which failure is excepted to occur (e.g., Fukuzono, 1985; Rose and Unger, 2006).

Although a linear fit is both practical and mathematically convenient, slope acceleration trending towards collapse/failure is rarely, if ever, linear when measured over a sufficient time-period (Rose and Unger, 2006).

Voight (1988) suggests that a power-law describing the terminal stages of failure should be reflected in other measurable (precursory) deformation including strain, seismicity rate, and seismic energy release. Early studies of precursory events leading to catastrophic failure focused on predicting earthquakes and volcanic eruptions (Byerlee, 1978; Voight, 1988).

Acoustic energy release is a natural by-product of intra- and inter-granular microcracking. Acoustic emissions rates measured in conventional triaxial rock-deformation experiments directly correlate to inelastic strain rates and are reliable indicators of approaching mechanical failure (Lockner & Byerlee, 1977; Lockner, 1993). In these experiments microcracks spatially concentrate late in the loading; near peak stress in a constant strain-rate experiment or at the onset of the tertiary creep phase in a constant-stress experiment (Lockner, 1993).

Natural examples of precursory inelastic strain events (damage accumulation) leading to slope-failures include a study of a chalk-cliff exposed along a shore in Western France where a power-law acceleration of both seismic rate and energy preceded a slope collapse (Armitrano, et al., 2005; Senfaute et al., 2009); and the study of a cliff exposed on the East coast of the U.K. where rockfall frequency and magnitude (volume) increased towards the time of slope failures (Rosser, 2007). Rosser (2007) also posits that both the rate and volume of precursory rockfall material could be proportional to the magnitude of the final failure volume. Kromer et al. (2015), documented both an increase in frequency of rockfalls leading to slope failure and a spatial coincidence of rockfall locations with the perimeter of the deforming rockmass.

The primary data used in this study are continuous recordings (24 hours per day, 15 frames per second) of thermal, infrared video of the monitored slope beginning roughly 5 days prior to an initial, slope collapse, and continuing to 27 days after a second collapse of the same slope. Thermal infrared cameras detect radiated heat energy and require no visible light (i.e., provide video imagery in both day and night conditions) and can provide a viable remote monitoring solution for both geotechnical hazards and situational awareness in surface mining environments (Wellman, et al., 2022). The selected thermal video camera (Teledyne FLIR ID-632 z 640 x 480 pixel, security camera) provides a 32-degree (horizontal) and a 26-degree (vertical) field of view (Figure 2-1). The entire pre-failure slope is within the thermal camera field of view except for a portion (lower-left) of the 2 lowermost, 50 ft (15.2 m) benches.

For several days leading to the Leo Failure, real-time interpretation of the thermal video data indicated an increase in frequency of rockfalls consistent with an increase in both displacement and acceleration observed in slope-monitoring radar data. Real-time monitoring also indicated that rockfalls appear to initiate along the perimeter of the future slope-failure boundaries.

Similar to Rosser (2007), this research documents an increase in number of rockfalls leading to the occurrence of both a large initial, slope failure (Leo Failure) occurring on May 31, 2021 (≈ 21 million tons) and a secondary slope failure (Leo-Scarp Failure) occurring on July 21, 2021.

We then use rockfalls, documented post-failure, to assess the viability of using rockfall frequency trends to predict the timing of the slope-failures. Finally, we present a viable but non-unique method to predict the timing of slope-failure based upon an observed systematic decrease in the time-interval between successive rockfalls.

2 Key Dataset and Description of Pre-Failure, Pit-Slope

The monitored pit-slope is within a porphyry copper mine in Utah, USA. Thermal camera monitoring was initiated on May 26, 2021 and continued to August 3, 2021. The pit-slope was selected for monitoring following a review of the mine-site, slope-monitoring sensors that indicated an acceleration of slope movement.

The mine elevation ranges from 4,000 ft (1200 m) to 7,000 ft (2130 m) above sea-level. The thermal camera was deployed across the pit, at an elevation of 6,200 ft (792 m). Figure 2-1 illustrates the scene observed from the camera in a thermal infrared image using a grayscale color-palette where lighter shades are thermally warmer. The camera field-of-view is directed south to a north-facing pit-slope. The bench increment is approximately 50 ft

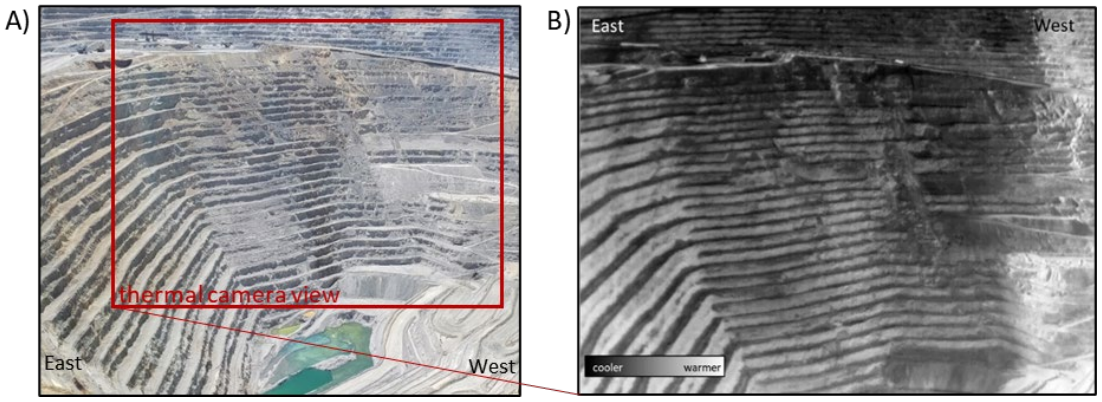

Figure 2-1. Photograph (A) and thermal image (B) of the monitored pit-slope prior to the initial slope-failure.

(15 m). Approximately 1,300 to 1,500 ft (400 m to 450 m) of vertical elevation is visible in the thermal camera field-of-view. The camera is located approximately 7,000 ft (2100 m) from the toe of the slope.

3 Description of the Leo Slope Failure

The north dipping inter-ramp angle of the slope prior to failure was between 37 and 38 degrees depending upon both slope azimuth and elevation. The initial slope-failure (Leo-Failure) occurred in multiple lithologies, including: quartzite, limestone, monzonite, and porphyritic quartz monzonite, P.Q.M. (Figure 3-1). The Leo Failure is bound

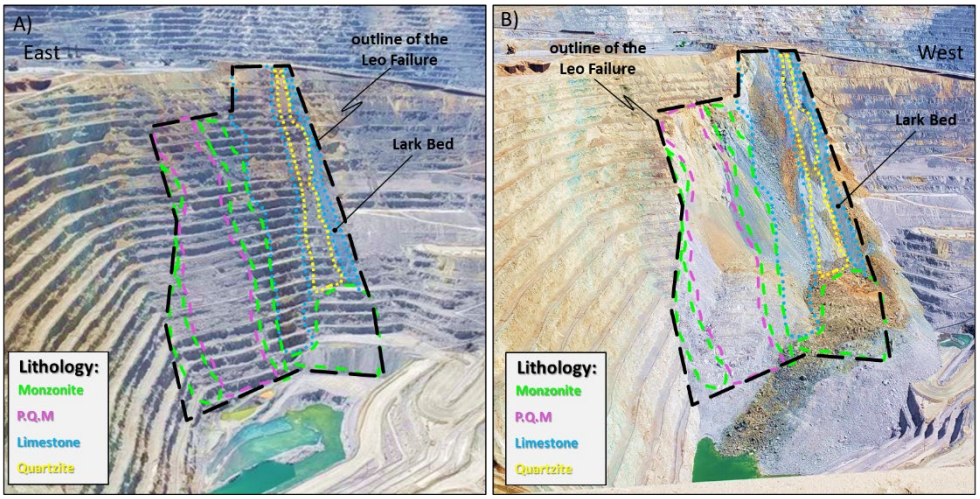

Figure 3-1. A) Photograph of the pit-slope prior to the Leo Failure with generalized lithologic units within the failure boundary. B) Photograph of the post-failure slope with generalized key lithologic units within the failure boundary.

to the West by the Lark Bed, a sedimentary, lithologic-contact reactivated as a fault with multiple phases of slip. The Lark Bed fault-core varies in thickness and includes sheared clay-sized gouge and clay minerals.

The primary slope failure occurred on May 31, 2021, in three stages or modes, initiating at the crest and generally propagating from the West to the East as the mass moved downslope. A first stage of failure ("Main Leo") is bound to the West by the Lark Bed and to the East by a contact of P.Q.M. with Monzonite. The secondary and tertiary blocks ("Left Leo") followed downslope and to the West, into the void left by the Main Leo mass (Figure 3-2). The total failure weight is approximately 21 million tons. Rockfalls were clustered on the side releases of the Main Leo failure boundaries (discussed in Section 4).

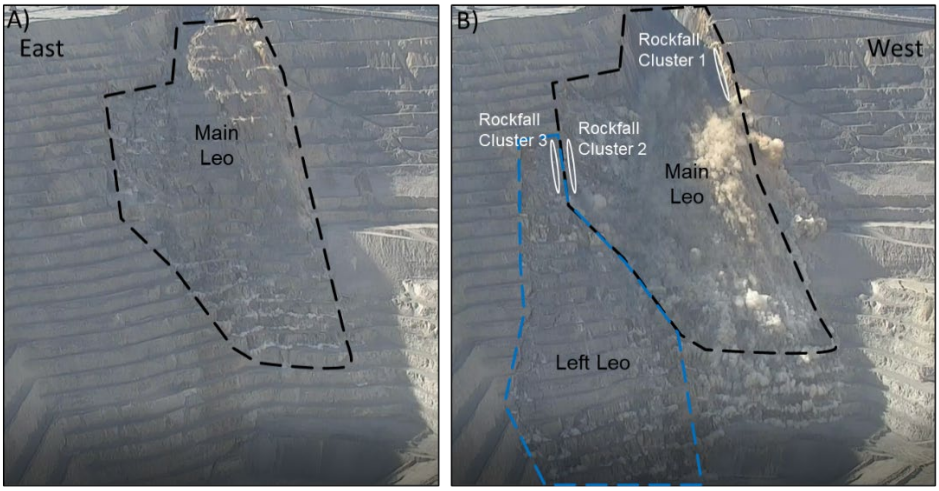

Figure 3-2. Photographs of the early stages of the Leo Failure. A) outline of the primary failure stage, Main Leo. B) Outline of the secondary to tertiary failure stages, Left Leo and locations of rockfall clusters prior to the failure**.**

4 Spatial and Temporal Analysis of Precursory Rockfalls

This section describes the occurrence (timing & location) of rockfalls leading to the Leo Failure on May 31, 2022 and a secondary failure of the Leo-Scarp on July 2, 2021.

4.1 Rockfalls Leading to the Initial, Leo Failure

Rockfalls can be discerned in thermal video images by the occurrence of thermal anomalies ('thermal scarring') associated with a ground disturbance that exposes either thermally cooler or thermally warmer rock with respect to the surrounding surficial temperature (Wellman, et al., 2022). The thermal anomaly could be related to several conditions including: plowing loose rock down the slope, generation of fine-grained dust, or fragmentation of either the falling or impacted rock. The estimated size of the falling rock is based upon the pixel resolution (in this case approximately 4-5 ft^2). In this dataset, there are very few instances for which the size of the actual falling rock can be discerned with confidence. Of the 158 documented rockfalls only 2 could be discriminated from the associated thermal scarring (2 pixels is approximately 9-10 ft^2). A systematic analysis of how many rockfalls occur that are either not detected by the thermal camera or were overlooked in the video analysis is not available. However, a preliminary review of higher-resolution thermal-videos (imaging portions of the same slope) yielded results consistent with thermal-camera video used in this analysis.

The estimated position of the origin of each of the 158 documented rockfalls are shown in Figure 4-1. The majority of rockfalls repeatedly originate from three primary areas (clusters) prior to the Leo slope failure and generally occur along the boundaries of the ultimate slope collapse with less than 10% originating from the center of the Main Leo segment. The right-most cluster 1 appears to be coincident with the Lark Bed (sedimentary contact reactivated as a fault), the future right-release of the Main Leo segment of the initial slope failure. Clusters 2 and 3 appear to be coincident with a location along the left-release of the Main Leo segment. Cluster 2 also appears to be positioned up-slope (within 100 ft) of a previous one to two-bench failure. Rockfalls do not appear to originate along the left release of the Left Leo segment of the failure. Origins of rockfalls generally elucidate the ultimate head-scarp of the failure but do not appear to define an initial break-out at the base of the slope failure (Figure 4-2).

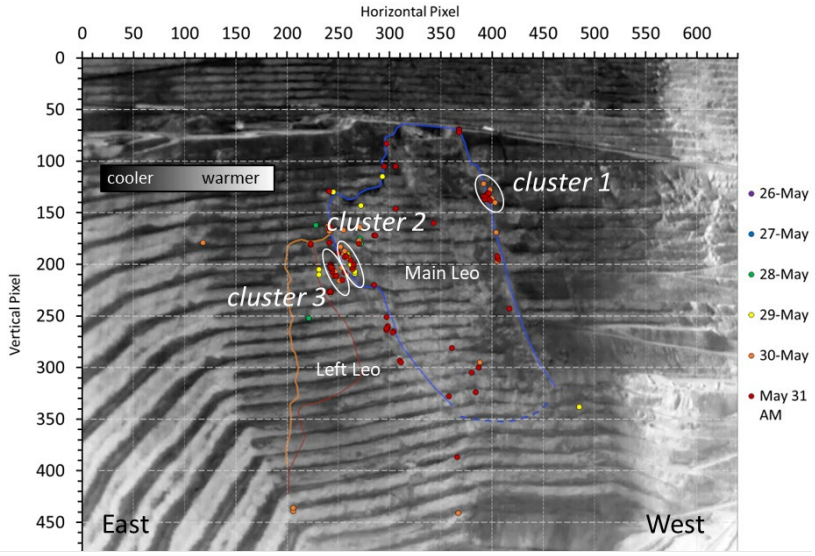

Figure 4-1. Image from thermal camera at approximately 7:30 AM, May 31 with locations of rockfalls occurring from May 26 to May 31. The failure stage boundaries are included.

Plotting the cumulative number of documented rockfalls vs time indicates that approximately 45% of the documented rockfalls occur within 6 hours of failure. The day-by-day sequential occurrence of initial rockfall positions are shown in Figure 4-3, spanning the same pre-failure time-interval as Figure 4-2. Spatial clusters of rockfalls are discernible from May 29 to May 30 and correspond to a relative increase in cumulative rockfalls (Figure 4-2). The interpreted origins of rockfalls appear to be spatially coincident with the outline of the top (crest),

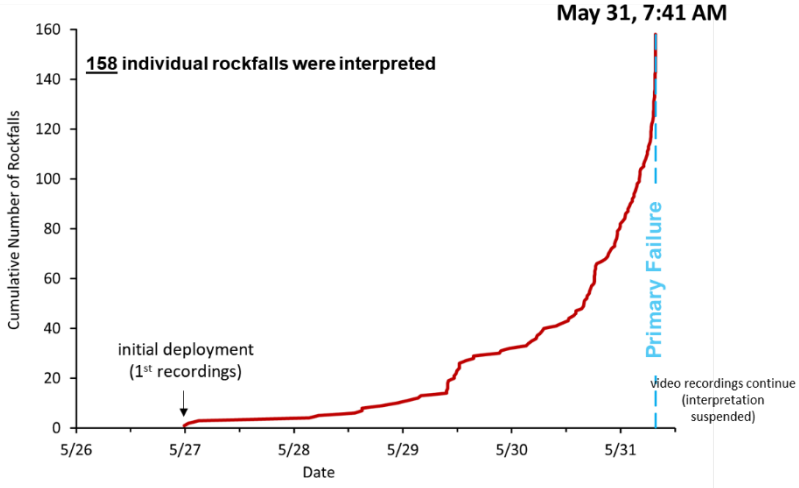

Figure 4-2. Plot of cumulative rockfalls vs time for the Leo Failure.

left-handed (East), and right-handed (West) releases of the primary failure stage of the Main Leo failure by the end of the day May 30, when the number of rockfalls begins to increase exponentially, up to the time of slope failure at 7:40 AM May 31, 2021. In the early morning hours of May 31, rockfalls began to originate more frequently from the 3 clustered locations but also at new positions down-slope, along the left and right releases; up-slope along the future head-scarp; and down-slope in the lower, central-portion of the Main Leo segment (See Figure 4-3, May 31 AM). Within the hour leading up to failure, the mean time between successive rockfalls is around 20 seconds, and within 2 minutes of failure, nearly a dozen rockfalls were documented.

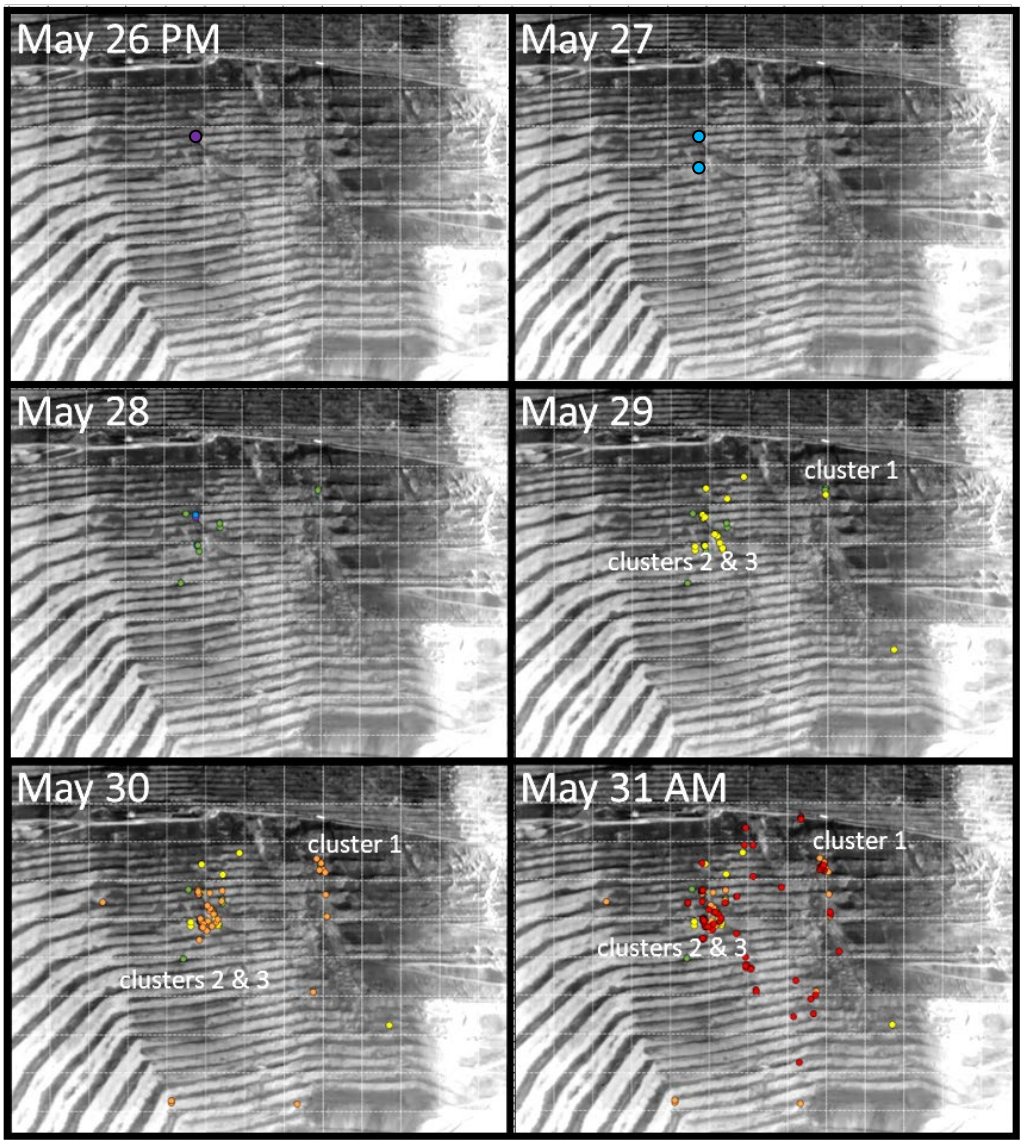

Figure 4-1. Still image at 7:30 AM on May 31 from thermal video with positions of rockfall origins for each day leading up the Leo Failure. The image is the same for each day shown.

4.2 Rockfalls Leading to the Secondary, Leo-Scarp Failure

The secondary, Leo-Scarp Failure occurred approximately 1 month after the Leo Failure in the upper portion of the scarp within the P.Q.M. lithologic unit. The failure mass was 100 ft (30 m) wide and 50 ft (15 m) in depth and

weighed approximately 35,000 tons. A total of 262 individual rockfalls were documented over the 4 days leading to a secondary collapse of the Leo scarp on July 2, 2021. The inferred origins of rockfalls appear to be spatially coincident with, and likely controlled by, the evolving morphology of the failure scarp. The majority of rockfalls originate along what appear to be, two channels in the talus slope of the Leo Scarp (Figure 4-4). Similar to the initial, Leo Failure, the cumulative number of rockfalls preceding the secondary failure increases exponentially within the hours leading to collapse with approximately 40% of the rockfalls occurring within 6 hours of collapse. However, for a similar time-interval (approximately 4 days) leading to failure, the total number of documented

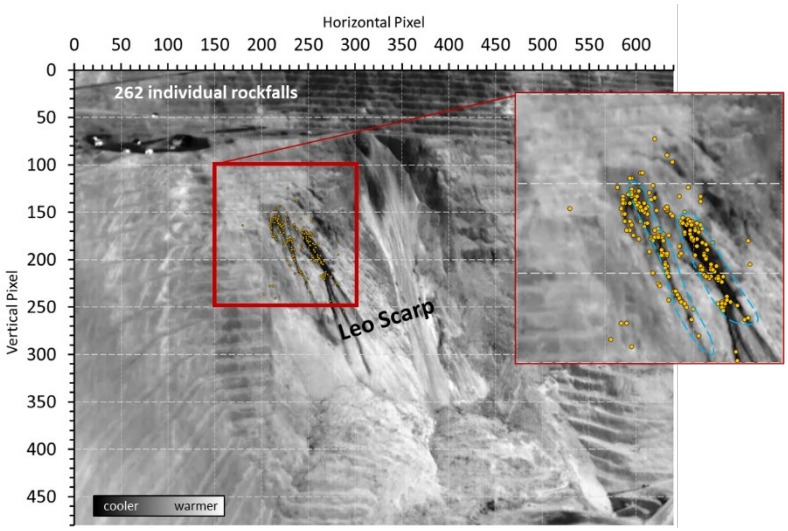

Figure 4-4. Image from thermal camera with locations of rockfalls occurring from June 29 to July 2, 2021. Darker (cooler) lineaments surrounding the failure are thermal scars due to a large amount of rockfalls and rock, debris flows along the boundaries of the unstable scarp.

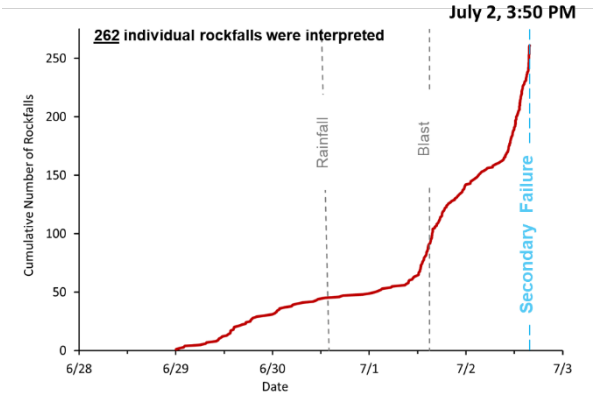

Figure 4-5. Plot of cumulative rockfalls vs time for the secondary failure of the Leo Scarp. Number of rockfalls documented, N = 262.

rockfalls is 262 (104 more than the Leo failure). The greater number of total rockfalls over a similar time interval leading to failure could be related to a relative weakening of the rock mass in the scarp by the rapid unloading of the initial-failure rock mass. The thermal video recorded both an excavation blast located at the working level (June 30, Figure 4-5) above the failure and a rainfall event (July 1, Figure 4-5). Neither event appears to have affected the frequency of documented rockfalls.

5 Discussion: Forecasting Slope Failure with Precursory Rockfalls

Multiple monitoring sensors, including synthetic aperture radar, were integrated to predict the time of the Leo Failure. Based upon selected radar data, the line-of-site cumulative displacement vs time (measured over the Main Leo area) appears to increase exponentially, consistent with a terminal, progressive phase of time-dependent deformation. The cumulative rockfalls vs time curve for both failures exhibit behavior similar to time-dependent, displacement curves (sensu Broadbent & Zavodni, 1982) where increases or decreases in rockfall frequency, may be considered a proxy for progressive or regressive stage developments, respectively. Comparing the Leo-Failure cumulative rockfalls vs time to the radar-displacement vs time, over the same time-period, at least 3 rockfall accelerations (progressive stages) can be interpreted prior to the final, progressive stage leading to the Leo Failure (Figure 5-1). In comparison to the initial Leo failure, 2 rockfall accelerations, each with a larger number of rockfalls (with respect to the initial Leo failure), can be interpreted prior to the final progression leading to the Leo Scarp failure. Both the initial Leo failure and the secondary, Leo-Scarp failure cumulative rockfalls vs time data can be described by fitting a smoothly varying exponential curve to the data (Figure 5-2). These results are similar to the results reported by Rosser et al., (2007) where precursory rockfalls were documented prior to the collapse of natural, limestone cliff located along the coast of the U.K.

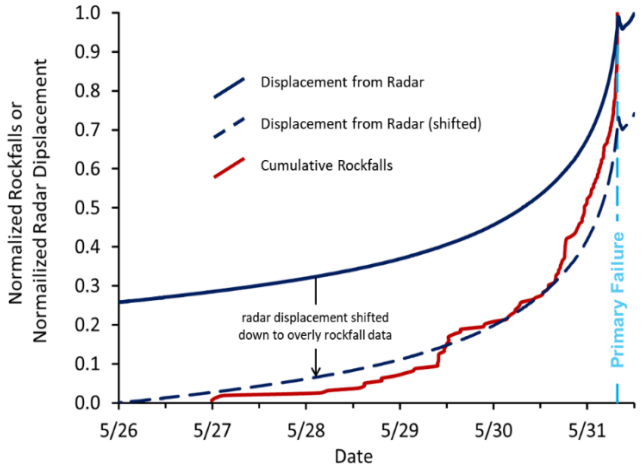

Figure 5-1. Normalized cumulative rockfalls vs time for the primary, Leo Failure and normalized radar-displacement data for the Main Leo segment of the failure.

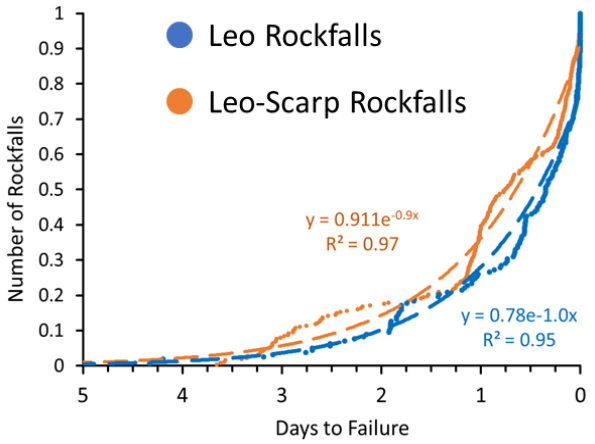

Figure 5-2. Normalized cumulative rockfalls vs days to failure for both primary, Leo and secondary, Leo-Scarp failures. Exponential regression trendlines are included for each rockfall dataset.

An aim of this study is to assess the viability of real-time monitoring of rockfall events to predict the timing of the ultimate slope collapse. Real-time prediction of failure timing is simulated by fitting (regressing) trends to abbreviated selections of the total documented rockfalls and comparing the time of failure predicted by the forward trend to the actual time of failure. A prediction is considered acceptable if the trend-curve is asymptotic within a few hours of the actual failure. The documented cumulative rockfalls indicate transient accelerations in the number of rockfalls, that could be interpreted as the terminal progression in a monitoring situation. A power-law regression of the first documented acceleration of rockfalls for the Leo Failure under-predicts the time of failure by approximately 1 day, whereas an exponential regression over-predicts the time of failure by up to 1 day. Both power-law and exponential trends through the first documented acceleration of rockfalls for the secondary, Leo-Scarp failure underpredict the time of failure by up to approximately 2.5 days (Figure 5-3 A). Considering a longer time-span of cumulative rockfalls, truncated at 4 days of observations (1 day prior to failure), power-law regressions underpredict the time of failure by approximately 0.5 days, whereas exponential regressions over-predict the time of the Leo Failure by up to 1 day and the Leo Scarp by up to approximately 0.5 days (Figure 5-3 B).

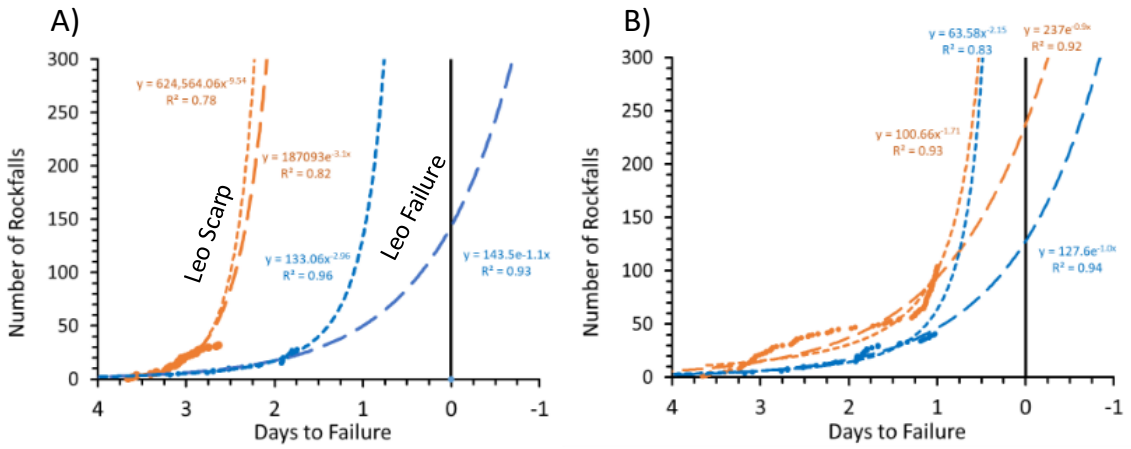

Figure 5-3. A) Cumulative rockfalls up to the time of the acceleration in rockfalls (progression) vs days to failure and both power and exponential trends fit to the truncated data. B) Cumulative rockfalls truncated at 4 days of observations (1 day prior to failure) and both power and exponential trend fit to the truncated data (blue-color data represent the Leo Failure and orange-color represent the Leo-Scarp).

The time-interval between successive rockfalls generally decreases with time leading to failure with punctuated transient acceleration periods (Figure 5-4). For example, on the 3rd day of recordings (3 to 2 days to the Leo Failure), the time interval between successive rockfalls ranged from 0.1 minutes to 341.7 minutes and averaged 71.0 minutes (Figure 5-4 A). Whereas over the 6 hours before failure the time interval between successive rockfalls ranged from 0.02 minutes to 36.7 minutes and averaged 4.9 minutes (Figure 5-4 A). Within the final

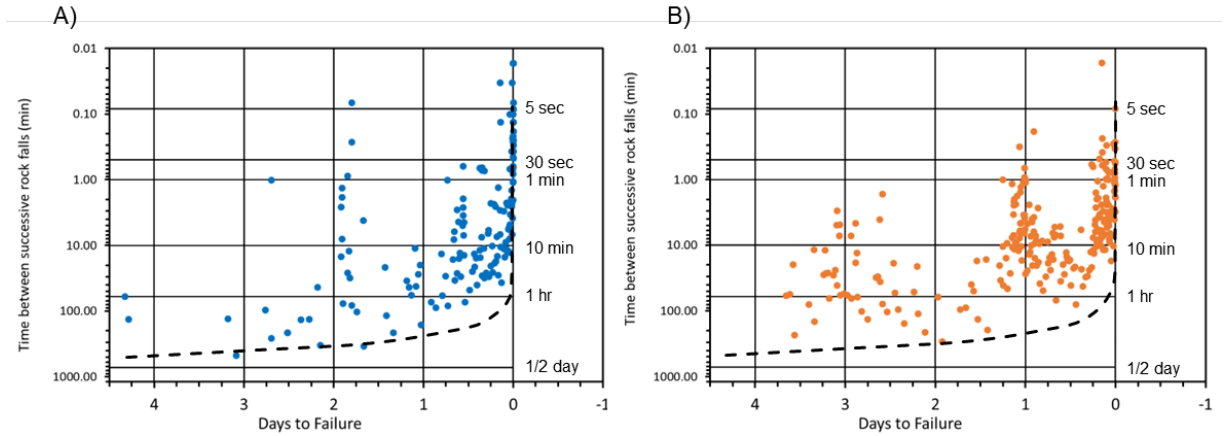

Figure 5-4. Time (in minutes) between each successive rockfall vs days to the initial, Leo Failure (A) and the secondary, Leo-Scarp failure (B). Note that the time interval decreases upward along the vertical, logarithmic axis. A power-law relationship that envelopes (bounds) the slowest time intervals between successive rockfalls is included in both (A) and (B).

hour of failure, the average time between successive rockfalls averaged 1.4 minutes with several rockfalls occurring less than 5 seconds of one another. A power-law relationship can be used to describe the systematic decrease in the maximum time (slowest time) between successive rockfalls leading to failure (Figure 5-4). The curve is positioned such that it effectively envelops the slowest time between successive rockfalls.

As with the cumulative rockfall data, real-time prediction of failure timing is simulated by fitting (regressing) trends to abbreviated selections of the total documented rockfalls and comparing the time of failure predicted by the trend-line to the actual time of failure. Data are plotted on a log-log scale with identical units of minutes and

power-law trends appear linear, thus providing a practical option of qualitative trend-fitting in a real-time scenario. The actual time of failure (on the horizontal axis) is considered to occur at 0.01 minutes or 0.6 seconds, which is effectively zero (see Figure 5-5). For the Leo Failure, a power-law trend line fit to a selection of the slowest time intervals between rockfalls, selected from the first 2 days of observations (3 to 4 days before failure) under-predicts the time of failure by approximately 5 hours (300 minutes). By considering an additional day of observations (total of 3 days) and revising the data selection the trend predicts the failure within several minutes. Including an additional day of observations (total of 4 days) does not appear to significantly improve the time of failure prediction.

For the Leo-Scarp failure, a power-law trend line fit to a selection of the slowest time intervals between rockfalls, selected from the first day of observations (3 to 3.5 days before failure) under-predicts the time of failure by approximately 1.2 hours (70 minutes). By considering an additional day of observations (total of 2 days) the trend predicts the failure within several minutes, but with a poor-fit (correlation coefficient 0.1). Including an additional 1.1 days of observations (total of 3.1 days) improves the time of failure prediction to within minutes of the actual failure with an improved correlation coefficient of 0.8. In this case, the exponent in the power law is nearly 1.0 and

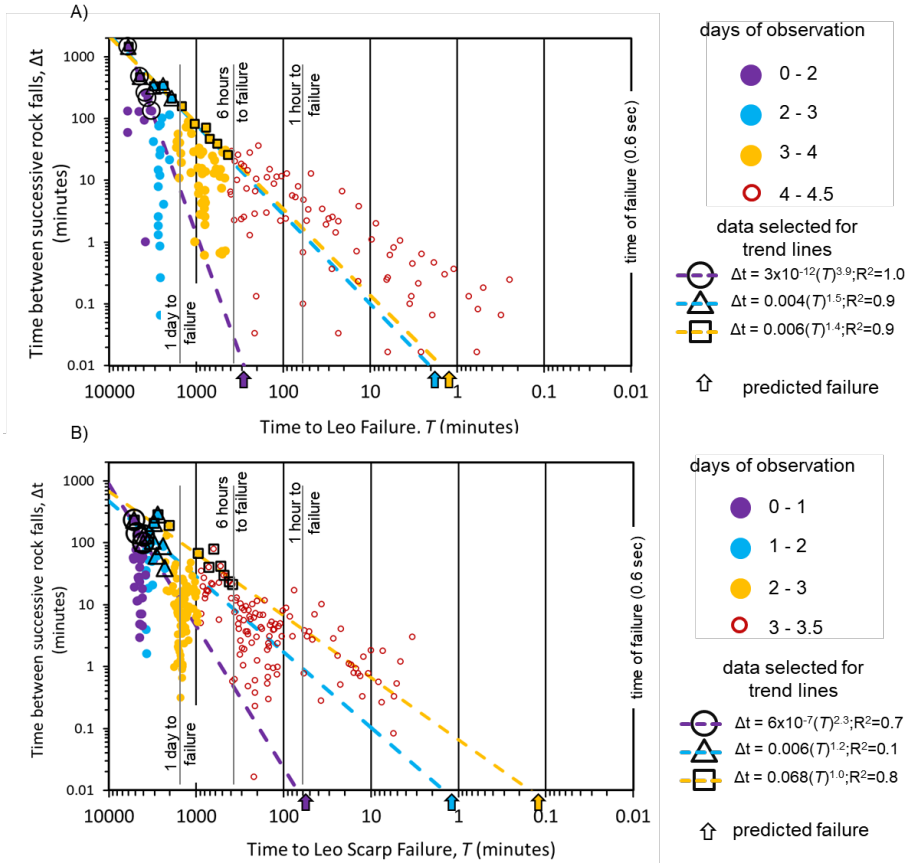

Figure 5-5. (A) Time (in minutes) between each successive rockfall vs minutes to the initial, Leo slope failure and the secondary, Leo-Scarp failure (B). Power-law trend-lines are fit to selected data and represent the slowest time between successive rockfalls. Unfilled symbols posted over filled-circles represent data selected for trend-line fitting. Data are plotted on a log-log scale with identical units and power-law trends appear linear.

the trend-fit is effectively linear. Data included in the trend-fitting exercise were truncated such that data within 6 hours of failure were not included. Additional data, within the 6 hours of failure, could be included in the trend-line prediction but are of lesser value in a real-time scenario where at least several hours are likely required to isolate the failing area from equipment and personnel. Although the trend-line exercise employed here predicted timing of failure within minutes of the actual failure, both the data selected for the trendline and the time-interval from which the data were selected are subjective (interpretative), making the predictions viable but non-unique. As with other methods of predicting timing of failure that include irreducible uncertainty (e.g., inverse-velocity method) a

more robust prediction will likely rely upon data integrated from a multitude of sources including multiple interpretations from several interpreters.

6 Summary & Conclusions

Continuous thermal video-recordings of rockfalls document the acceleration of precursory deformation leading to two slope failures; an initial failure followed, 32 days later, by a second slope failure. For both failures, the cumulative number of recorded rockfalls increases (considered over a 4 to 4.5 day time span) according to either an exponential or power-law relationship. Approximately 45% of the total interpreted rockfalls (158) occurred 6 hours prior to the initial, Leo Failure. In the 3-4 days leading up to the secondary failure a similar cumulative rockfall behavior is documented with approximately 40% of the total interpreted rockfalls (262) occurring in the 6 hours leading up to the secondary failure.

Based upon fitting (statistical regression) both power and exponential trends to cumulative rockfall data a predictive relationship was developed to estimate the time of failure. The power-law trends appear to underpredict the failure time by as little as approximately 12 hours. The exponential trends appear to over-predict the time of failure by as little as approximately 8 hours.

The preferred method to predict time of failure considers the systematic decrease in the maximum time-interval between rockfalls. A power-law relationship can be fit (statistical regression) to selected rockfall events to provide a viable but non-unique prediction of the time of failure. The method relies upon subjective or biased sampling of data prompting further scrutiny or validation with additional studies of precursory rockfalls leading to failure.

Future research should include developing thermal video systems that include automated rockfall detection and tracking algorithms. This would likely increase the capabilities of thermal-video as a real-time monitoring tool that could deployed alongside traditional slope-monitoring systems (e.g., total station – prism systems and radar systems). Continuing this research on rockfall detection and failure prediction has the potential to save lives in mining, civil, and natural environments.

7 Acknowledgements

This research was conducted with the support of a NIOSH Research Grant (NIOSH BAA#: 75D301-20-R-67845). The GCE also would like to acknowledge the permission to publish data acquired at Rio Tinto Kennecott Copper. Their support of this project and research to improve mine safety is gratefully acknowledged. The manufacturer's names in this report are provided for reference only. The use of manufacturer specifications and data is for information only. It does not constitute an endorsement by the University of Arizona, Lowell Institute for Mineral Resources, Rio Tinto, NIOSH, CDC, or the US Government.

8 References

Armitrano, D., Grasso, J.R., & Senfaute, G. (2005). GEOPHYSICAL RESEARCH LETTERS, VOL. 32, L08314, doi:10.1029/2004GL022270,

Broadbent, C. D and Zavodni, Z. M. (1982). Influence of Rock Structures on Stability, in Stability in Surface Mining, Society of Mining Engineers, Denver, Co. Vol.3, Ch.2.

Byerlee, J. (1978) Friction of Rocks. Pure and Applied Geophysics, 116, 615–626

Fukuzonu, (1985) Inverse Velocity Over Time A New Method for Predicting the Failure Time of a Slope, Proceedings of the IVth International Conference and Field Workshop on Landslides, Tokyo, Japan

Hobbs,, B.E. (1976) An Outline of Structural Geology, John Wiley & Sons.

Hoek, E. (1983). Strength of jointed rock masses. *Géotechnique* 33: 187–223.

Kromer, R.A., Hutchison, D.J., Lato, M.J. & Gauthier, D. (2015) Identifying Rock Slope Failure Precursors Using LiDAR for Transportation Corridor Hazard Management. Engineering Geology 195.

Lockner, D. (1993) Room Temperature Creep in Saturated Granite. Journal of Geophysical Research: Solid EarthVolume 98, Issue B1 p. 475-487

Lockner, D. and Byerlee, J.D. (1977). Hudrofracture in weber sandstone at high confining pressure and differential stress. Journal of Geophysical Research 82Read, J., Stacey, P. (2009). *Guidelines for Open Pit Slope Design*. CSIRO Publishing, Collingwood.

Rose, N. D. and Hungr, O. (2006). “Forecasting potential slope failure in open pit mines – contingency planning and remediation”, International Journal of Rock Mechanics and Mining Sciences, 44 (2007)

Rosser, N., M. Lim, D. Petley, S. Dunning, and R. Allison (2007), Patterns of precursory rockfall prior to slope failure,J. Geophys. Res.,112, F04014, doi:10.1029/2006JF000642

Senfaute, G., Duperret, A., and Lawrence, J. A. (2009). “Micro-seismic precursory cracks prior to rock-fall on coastal chalk cliffs: a case study at Mesnil-Val, Normandie, NW France”, Nat. Hazards Earth Syst. Sci., 9, 1625–1641.

Voight, B.A. (1988) A method for prediction of volcanic eruptions. Nature 332, 125-130.

Wellman, E.C., Schafer, K.W., Williams, C.P. & Ross, B.J. (2022). Thermal Imaging for Rockfall Detection. American Rock Mechanicas Association, Annual Meeting, Santa Fe. ARMA 22-430.

Zavodni, Z.M. (2001) Time-Dependent Movements of Open-Pit Slopes. SME Proceedings, Denver, Colorado, pp. 81-87.